Three Dimensional End-to-End Modeling and Directivity Analysis for Graphene-based Antennas in the Terahertz Band

Chuanji Zhang, **Chong Han** and **Ian F. Akyildiz**
Broadband Wireless Networking Laboratory
School of Electrical and Computer Engineering
Georgia Institute of Technology, Atlanta, Georgia 30332, USA
Email: {jenny.zhang, chong.han, ian}@ece.gatech.edu

***Abstract*—Terahertz (0.1-10 THz) band communication is envisioned as a key technology to satisfy the increasing demand for ultra-high-speed wireless links. In this paper, a three dimensional (3D) end-to-end model is developed, which includes the graphene-based antenna response and the channel model in the THz band. The developed theoretical model is validated with COMSOL simulations. By using the developed 3D end-to-end model, an in-depth analysis on the 3D channel characteristics is carried out. In particular, the use of a 13-dB-gain antenna leads to the decrease of the delay spread from 0.2 ns to 3.2 ps, and the decrease of the angular spread by a factor of 20. The resulting coherence bandwidth reaches 63 GHz. A target capacity of 100 Gbps can be achieved with the directional antenna for the distance of 0.4 m over 0.8-0.9 THz, which is unreachable with the isotropic antenna. However, the directivity is at the cost of the strict antenna alignment, and the deviation needs to be smaller than 12.4°. The provided analysis lays out the foundation for reliable and efficient ultra-high-speed wireless communications in the THz band.**

I. Introduction

With the rapid penetration of wireless communications in our daily lives, wireless data traffic has been going through an exponentially increase over the past decades. Over the last three decades, the wireless data rates have doubled every eighteen months [1]. In order to satisfy the increasing demand for data rate, new spectral bands are required. Amongst others, the Terahertz band, i.e., (0.1-10) THz is considered as one of the most promising spectrum bands to support high speed wireless communications in the future. With its ability to offer an ultra-broad bandwidth and support very high data rates, the THz band is attracting increasing attention in recent years [2].

Existing THz-band channel models in [3], [4] are developed for 2D cases where the EM waves traveling only in the azimuth plane are considered. Due to 2D modeling, the propagation effects in the elevation plane are not captured. In the realistic application scenarios, the multi-path rays reach the receiver from both the azimuth and elevation planes. This is the result of the 3D radiation diagram of the antennas and the 3D propagation of the waves in free space. These facts change the analysis on the delay spread, the coherence bandwidth, the angular spread, and the channel capacity. Consequently, there is a need for a 3D end-to-end model, which captures the influences of the antenna response and multipath propagation on the channel characteristics.

Intrinsic material properties of metals remain unknown at the nanoscale [5]. In recent years, the new nano-material graphene based antennas are becoming increasingly well accepted to be used for very high frequencies such as (0.1-10) THz band. Also the graphene based antennas are developed and about to be fabricated in the research world [6]. To provide the directivity gain with the graphene antenna, a reflector can be added behind the graphene-based nano-antenna [7]. With this configuration, although the graphene antenna is in the nano-scale, the size of the transmitter, including the reflector is much larger and is able to provide more than 10 dB antenna gain. Even with the directivity, the antenna radiation pattern has 3D beamwidth, which results in the fact that the 3D multi-path effect still exists but is confined in the radiation sector. Within this perspective, the antenna gain and beamwidth, and the antenna misalignment effects need to investigated.

In this paper, the contributions are summarized as follows. First, we develop a 3D end-to-end model, which includes the graphene-based antenna response and the EM wave propagation channel in the THz band. The theoretical model is validated with COMSOL Multiphysics simulations [8]. Then, we present an in-depth analysis on the 3D channel characteristics in the THz Band. In particular, we thoroughly characterize the antenna gain and beamwidth, the power angle profile, the power delay profile and the coherence bandwidth, the channel capacity, and the antenna misalignment effects.

The rest of the paper is organized as follows. In Section II, a 3D end-to-end channel model in THz band is developed. Moreover, the validation of the antenna response is provided. Then, the characteristics of the 3D channel in the THz band are analyzed using the developed model in Section III. Finally, the paper is concluded in Section IV.

II. A 3D End-To-End Propagation Model

In this section, we develop a 3D end-to-end model, which captures the EM wave propagation in a 3D environment from the transmitting to the receiving antenna in the (0.1-10) THz band. Since the wave propagation in the THz band is frequency-dependent, the model is developed as a combination

978-1-4799-5952-5/15/$31.00 ©2015 IEEE

of a number of sub-bands, which are narrow enough to be considered as flat fading channels. The operating frequency, f, takes values of $\{f_1, f_2 \ldots, f_n, \ldots\}$, where f_n is the center frequency of the n^{th} sub-band. The bandwidth of each sub-band is identical and equal to $\Delta f = f_{n+1} - f_n$.

In the end-to-end channel model, multiple rays travel from the transmitting to the receiving antenna. Accordingly, the transfer function $H_{\mathrm{e2e}}(f)$ of the end-to-end model is the sum of the transfer function of all i rays, where

$$H_{\mathrm{e2e}}(f) = \sum_{i=1}^{I} A_T^{(i)}(f) H^{(i)}(f) A_R^{(i)}(f), \tag{1}$$

where A_T and A_R denote the frequency responses of the transmitting and receiving antennas. H refers to the transfer function of the THz band channel. I is the total number of multipath components, which decreases with the reducing antenna beamwidth. In the sequel, we describe the characteristic of each term in the above model.

A. Frequency Response of Graphene-based Nano-antennas

The frequency response of the graphene-based antenna at the transmitter is given by

$$A_T^{(i)}(f) = \sqrt{e_T(f) D_T(f, \theta_{AOD}, \phi_{AOD})}, \tag{2}$$

where e_T is the transmitting antenna radiation efficiency, mainly depending on the material of antenna, the feeding scheme, and the operating frequency. In this work, we assume the antenna efficiency with a plasmonic excitation source as 30% as suggested in [7]. D_T stands for the directivity of the transmitting antenna, which is a function of the frequency. θ_{AOD} is the elevation angle of departure (AOD) and ϕ_{AOD} is the azimuth angle of departure (AOD). The directivity D_T is

$$D_T(\theta, \phi) = \frac{4\pi U(\theta, \phi)}{P_{rad}}, \tag{3}$$

where $U(\theta, \phi)$ is the radiation intensity at the distance d

$$U(\theta, \phi) \approx \frac{d^2}{2\eta} [|E_\theta^t(\theta, \phi)|^2 + |E_\phi^t(\theta, \phi)|^2], \tag{4}$$

and P_{rad} is the total radiated power,

$$P_{rad} = \int_0^{2\pi} \int_0^{\pi} U(\theta, \phi) \sin(\theta) d\theta d\phi. \tag{5}$$

In (4) and (5), η denotes the intrinsic impedance of the medium, $E_\theta^t(\theta, \phi)$ and $E_\phi^t(\theta, \phi)$ refer to the total polar and azimuthal far-zone electric-field vector components, respectively. The configuration of the graphene-based reflector antenna is considered for directivity, by which a graphene antenna is put in front of a nearly no-loss reflector. By adding a reflector in front of the patch, the electromagnetic waves can be reflected to a desired direction and thus, can achieve the function of a directional antenna. The total far-field electric fields are

$$E_\phi^t(\theta, \phi) = E_\phi(\theta, \phi) \times R_F(\theta, \phi), \tag{6}$$

$$E_\theta^t(\theta, \phi) = E_\theta(\theta, \phi) \times R_F(\theta, \phi), \tag{7}$$

where R_F is the field factor contributed by the reflector, which depends on the shape and position of the reflector. In the above equation, the polar and azimuthal far-zone electric-field components $E_\theta(\theta, \phi)$ and $E_\phi(\theta, \phi)$ of the graphene antenna are given by

$$E_\theta(\theta, \phi) \approx 0, \tag{8}$$

$$E_\phi(\theta, \phi) = j \frac{k L_h L_w E_0 \mathrm{e}^{-jkd}}{2\pi d} \sin(\theta) \frac{\sin(X)}{X} \frac{\sin(Y)}{Y} \times 2\cos(\frac{kL_l}{2} \sin\theta \cos\phi), \tag{9}$$

where $X = \frac{kL_h}{2} \sin\theta\cos\phi$, $Y = \frac{kL_w}{2} \cos\theta$, and L_h, L_w, and L_l are the height, width, and length of the graphene patch, respectively. In particular, the height is much less than the width, i.e., $L_h \ll L_w$. E_0 is the electric field across L_h. As a result of the small Surface Plasmon Polariton (SPP) wavelength along graphene [6], $\frac{\sin X}{X}$, $\frac{\sin Y}{Y}$ and $\cos(\frac{kL_l}{2} \sin\theta\cos\phi)$ can be approximated to be 1. Then, the azimuthal far-zone electric-field in (9) can be further rearranged as

$$E_\phi(\theta, \phi) \approx \frac{k L_h L_w E_0 \mathrm{e}^{-jkd}}{2\pi d} \sin(\theta). \tag{10}$$

In this work, we consider a 30° and 90° corner reflector. By denoting l as the distance from the patch to the vertex and α as the included angle, the field factor for 30° and 90° corner reflector is expressed as

$$\begin{aligned} R_F(\theta, \phi) =& 2[(-1)^a \cos(P) - 2\cos[\cos(\alpha)P] \cos[\sin(\alpha)Q] \\ & - (-1)^a \cos(Q) + 2\cos[\sin(\alpha)P] \cos[\cos(\alpha)Q]] \end{aligned} \tag{11}$$

where $P = kl\sin\theta\cos\phi$, $Q = kl\sin\theta\sin\phi$, and a=1 for $\alpha = 90°$, a=2 for $\alpha = 30°$.

On the other hand, the frequency response of the graphene antenna at the receiver is computed as:

$$A_R^{(i)}(f) = \sqrt{e_R(f) D_R(f, \theta_{AOA}, \phi_{AOA}) \frac{\lambda^2}{4\pi}}, \tag{12}$$

where e_R is the receiver antenna radiation efficiency. D_R is the directivity of the receiving antenna, which is a function of frequency, the elevation angle of arrival (AOA), θ_{AOA}, and the azimuth angle of arrival (AOA), ϕ_{AOA}. The directivity of the receiving antenna can be obtained in a similar way as for the transmitting antenna in (3).

B. 3D Channel Model in the Terahertz Band

In this section, we develop the THz 3D channel model with the line-of-sight (LoS), reflected and scattered paths. The geometry configuration is demonstrated in Fig. 1, where the traveling distance of the i^{th} ray is given by

$$L_i = \begin{cases} d & \text{LoS} \\ r_1 + r_2 & \text{Reflected Rays} \\ s_1 + s_2 & \text{Scattered Rays} \end{cases} \tag{13}$$

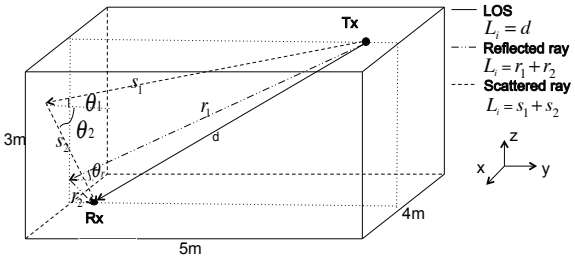

Figure 1: The multipath propagation model between the transmitter (Tx) and the receiver (Rx).

where d is the direct distance between the transmitter and the receiver. r_1 is the distance from the transmitter to the reflector, and r_2 is the distance from the reflector to the receiver. s_1 is the distance from the transmitter to scattering point, and s_2 is the distance between the scattering point to the receiver.

The channel frequency response function for the i^{th} ray in the n^{th} sub-band is given in (14) on the next page. In this equation, $\tau_i = L_i/c$ is the time-of-arrival of the ray and c denotes the speed of light. k_{ma} is the frequency-dependent medium absorption coefficient, which depends on the composition of the transmission medium [9]. In the reflected ray model, the Fresnel reflection coefficient γ for the transverse electric (TE) polarized waves on a smooth surface is obtained as

$$\gamma_{\text{TE}}(f) \approx -\exp\left(\frac{-2\cos(\theta_{\text{r}})}{\sqrt{n_t^2-1}}\right), \tag{15}$$

where θ_{r} is the angle of incident wave and can be computed using the law of cosine, i.e., $\theta_r = \frac{1}{2}\cos^{-1}\left(\frac{r_1^2+r_2^2-d^2}{2r_1r_2}\right)$. n_t refers to the refractive index, varying with the frequencies and reflecting material. In order to characterize the effect of the surface roughness, a Rayleigh factor [10] is introduced as

$$\rho(f) = \exp\left(-\frac{8\pi^2\cdot f^2\cdot\sigma^2\cdot\cos^2(\theta_{\text{r}})}{c^2}\right), \tag{16}$$

where σ is the rough surface height standard deviation. In the scattered ray model, the scattering geometry is considered on the tangent plane (the incident azimuth angle ϕ_1 is π), and θ_1 stands for the zenith angle of the incident wave. In addition, θ_2 and ϕ_2 denote the zenith and azimuth angles of the scattered wave, respectively. The scattering coefficient $S(f)$ of rough surfaces according to the modified Beckmann-Kirchhoff theory [11] is given by

$$\begin{aligned} S(f) &= \gamma_{\text{TE}}(f)\cdot \text{e}^{-\frac{g}{2}}\cdot\sqrt{\rho_0^2+\frac{\pi L_c^2F^2}{l_xl_y}\sum_{m=1}^{\infty}\frac{g^m}{m!m}\text{e}^{-v_s/m}} \\ &\approx -\exp\left(\frac{-2\cos(\theta_1)}{\sqrt{n_t^2-1}}\right)\cdot\sqrt{\frac{1}{1+g+\frac{g^2}{2}+\frac{g^3}{6}}} \\ &\quad\cdot\sqrt{\rho_0^2+\frac{\pi\cos(\theta_1)}{100}\left(g\text{e}^{-v_s}+\frac{g^2}{4}\text{e}^{-v_s/2}\right)} \end{aligned} \tag{17}$$

The parameters in this model are

$$g = k^2\sigma^2\left(\cos(\theta_1)+\cos(\theta_2)\right)^2, \tag{18}$$

$$\rho_0 = \text{sinc}(v_xl_x)\cdot\text{sinc}(v_yl_y), \tag{19}$$

$$l_x = l_y = 10L_c, \tag{20}$$

$$v_x = k\cdot\left(\sin(\theta_1)-\sin(\theta_2)\cos(\phi_2)\right), \tag{21}$$

$$v_y = k\cdot\left(-\sin(\theta_2)\sin(\phi_2)\right), \tag{22}$$

$$v_s = (v_x^2+v_y^2)L_c^2/4, \tag{23}$$

where L_c is the correlation length of the rough surface, and the geometrical factor $F^2 = \cos(\theta_1)$ is suitable for large incidence and scattering angles. In the above derivations, we used Taylor's approximation to simplify the expression for the scattering coefficient.

C. Validation

The theoretical 3D end-to-end model in (1) consists of the graphene antenna response and the multipath propagation model. The multipath propagation model in the THz band in (14) was validated in [4]. Hence, in this section, we focus on the validation of the 3D graphene antenna response in (2). Specifically, we utilize COMSOL Multiphysics to simulate the graphene antenna response and validate the theoretical model of 3D radiation pattern in (2) with the simulation results. The geometric configuration of the graphene antenna with a reflector is shown in Fig. 2(a). The normalized radiation pattern of the graphene antenna in the azimuth and elevation planes at f =1 THz using this configuration is plotted in Fig. 2(b).

For the azimuth plane, the theoretic solution (7) fits well with the simulation results at the main lobe. The 3 dB beamwidth for the azimuth plane is around 26°. The sidelobes appear in the simulations since the COMSOL does not consider the reflector length infinite for R_F as in the theoretical derivation in (11). Thus, the radiation leaking from the aperture causes the sidelobes. However, this has negligible effects on our analysis since the sidelobe attenuation is more than 40 dB. For the elevation plane, the theoretical model and the simulation results match well. The mismatch occurs because the height of the reflector is finite and the material of the reflector is not perfect for reflection in COMSOL.

III. 3D Channel Characterization

Using the developed propagation model, we present a detailed analysis of the 3D end-to-end channel characteristics in the THz Band. In particular, we thoroughly characterize the antenna gain and beamwidth, the power angle profile, the power delay profile and the coherence bandwidth, the channel capacity, and the misalignment effects. We can improve the system performance when the graphene-based antennas are used. However, the use of the directional antenna requires the beam alignment between the transmitter and the receiver.

A. Antenna Gain and Beamwidth

The achieved gain and beamwidth of the graphene-based reflector antenna depends on the ratio between l, and the

$$H^{(i)}(f) = \begin{cases} \left| \frac{c}{4\pi \cdot f \cdot d} \mathrm{e}^{-\frac{1}{2}k_{\mathrm{ma}}(f)d} \right| \cdot \exp\left(-j2\pi f \tau_i\right) & \text{LoS} \\ \left| \left(\frac{c}{4\pi \cdot f \cdot (r_1+r_2)}\right) \mathrm{e}^{-\frac{1}{2}k_{\mathrm{ma}}(f)(r_1+r_2)} \cdot \gamma_{\mathrm{TE}}\left(f_n\right) \cdot \rho\left(f\right) \right| \cdot \mathrm{e}^{-j2\pi f \tau_i} & \text{Reflected Rays} \\ \left| \left(\frac{c}{4\pi \cdot f \cdot (s_1+s_2)}\right) \mathrm{e}^{-\frac{1}{2}k_{\mathrm{ma}}(f)(s_1+s_2)} \cdot \left(-\mathrm{e}^{\frac{-2\cos(\theta_1)}{\sqrt{n_t^2-1}}}\right) \cdot S(f) \right| \cdot \mathrm{e}^{-j2\pi f \tau_i} & \text{Scattered Rays} \end{cases} \tag{14}$$

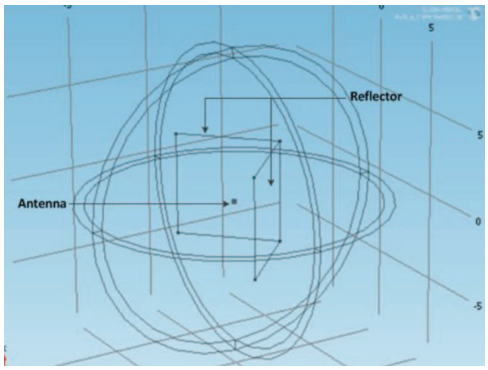

(a) Antenna configuration in COMSOL

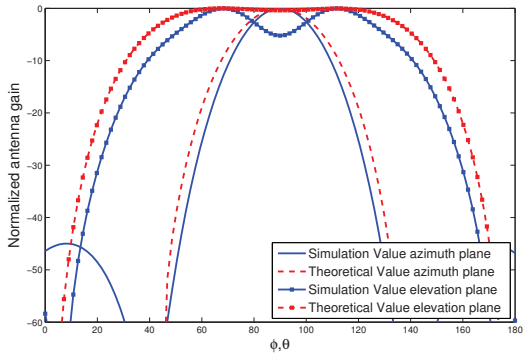

(b) Normalized gain

Figure 2: A graphene antenna and the normalized gain.

wavelength, λ. It is also related to α. In general, with the same input power, the gain increases while the beamwidth becomes narrower. In Table I, we give the antenna gain, and the beamwidth for different operating frequencies and different configurations of the graphene-based reflector antenna.

The results indicate that when l/λ and α are fixed, the radiation patterns are the same at different operating frequencies. For example, the gain is 6.3 dB and the 3 dB beamwidths are 40° and 76°, when $l = 0.5\lambda$ and $\alpha = 90^\circ$. In addition, the use of reflector with $\alpha = 30^o$ narrows the 3 dB beamwidths to 15^o and 38^o for the azimuth and elevation planes, and increases the gain by 7 dB. This is expected since a smaller angle reflector introduces better directional characteristic due to its angle narrowness. Furthermore, for the same frequency, the case when $l = 0.5\lambda, \alpha = 90^o$ and the case when $l = 0.7\lambda, \alpha = 90^o$ have the same gain. However, the radiation pattern and the 3 dB beamwidths differ. For example, the case with $l = 0.7\lambda$ has a narrow beam in the azimuth plane and a wide pattern in

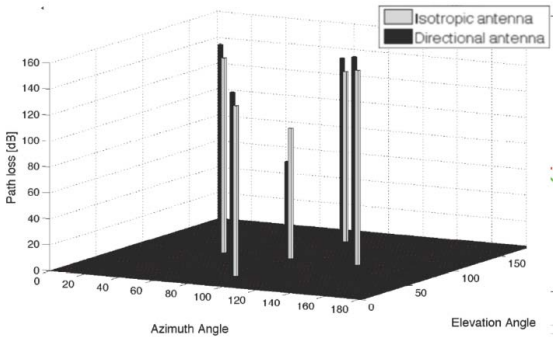

Figure 3: Power angle profile of 3D end-to-end channel.

the elevation plane. Therefore, the gain and beamwidth of the graphene-based reflector antenna can be adjusted according to the different requirements for the gain and beamwidth.

B. Power Angle Profile

Power angle profile (PAP) is an important factor to study the spatial characteristics of the channel, which is critical for the beam alignment between the transmitter and receiver. We study the PAP for both the elevation (θ) and azimuth (ϕ) arrival angles. In a room of dimensions $5\mathrm{m} \times 4\mathrm{m} \times 3\mathrm{m}$, the transmitter and receiver are located on ceiling and floor as shown in Fig. 1. The PAPs for the uses of isotropic antenna and the directional antennas at the operating frequency of 0.5 THz are shown in Fig. 3, in which the significant rays include the LoS and the four clusters of the reflected and scattered rays. We define the rms angular spread as

$$\sigma_{angle}(f) = \sqrt{\overline{\theta^2}(f) - \left(\overline{\theta}(f)\right)^2}, \tag{24}$$

$$\overline{\theta^x}(f) = \frac{\sum_{i=1}^{I} |\alpha_i(f)|^2 |\theta_i|^x}{\sum_{i=1}^{I} |\alpha_i(f)|^2}, \tag{25}$$

where $\overline{\theta^x}$ describes the first (x=1) or second (x=2) moment of the instantaneous power-angle profile, respectively. α_i is the amplitude of the i^{th} path in the frequency domain, which is $\alpha_i(f) = |A_T^{(i)}(f) H^{(i)}(f) A_R^{(i)}(f)|$ in (1).

When the isotropic antennas are used, the rms angular spread for azimuth and elevation plane are 16.7^o and 25.2^o. The strongest NLoS ray has a 31 dB attenuation compared to the LoS path. When the directional antennas are used, the rms angular spread reduces to 0.8^o and 1.2^o for azimuth and elevation plane, which is around 95% decrease compared with the isotropic antenna case. Moreover, the strongest NLoS ray has 57 dB less power than the LoS path in this case.

Table I: Antenna Gain and Beamwidth

	$f = 0.5$ THz			$f = 1$ THz		
	$l = 0.5\lambda$ $\alpha = 90^o$	$l = 0.7\lambda$ $\alpha = 90^o$	$l = 0.5\lambda$ $\alpha = 30^o$	$l = 0.5\lambda$ $\alpha = 90^o$	$l = 0.7\lambda$ $\alpha = 90^o$	$l = 0.5\lambda$ $\alpha = 30^o$
Gain [dB]	6.3	6.3	13.4	6.3	6.3	13.4
3 dB Beamwidth azimuth plane	40^o	38^o	15^o	40^o	38^o	15^o
3 dB Beamwidth elevation plane	76^o	106^o	38^o	76^o	106^o	38^o

Table II: Power Delay Profile

		Isotropic antenna (with LoS)	Directional antenna (with LoS)	Directional antenna (no LoS)
	Time of Arrival [ns]	Path Gain [dB]	Path Gain [dB]	Path Gain [dB]
LoS	16.7	-100.6	-74.6	-
Reflected Ray 1	21.3	-131	-141	-105
Reflected Ray 2	21.3	-131	-141	-151
Reflected Ray 3	19.4	-150	-160	-170
Scattered Ray 1	21.36	-142	-152	-117
Scattered Ray 2	21.40	-145	-155	-120

C. Power Delay Profile and Coherence Bandwidth

With the same system setup described in Section III-B, the power delay profiles of an isotropic antenna and a 13 dB directional antenna at the transmitter and the receiver are studied, and the simulation results are summarized in Table II. Moreover, the total power gain, the rms delay spread and the coherence bandwidth are calculated for the different cases.

For the LoS cases, the total power gain increases from -100.59 dB to -74.6 dB when the directional antenna is used. The rms delay spread is defined as

$$\sigma_{delay}(f) = \sqrt{\overline{\tau^2}(f) - (\overline{\tau}(f))^2}, \tag{26}$$

$$\overline{\tau^x}(f) = \frac{\sum_{i=1}^{I} |\alpha_i(f)|^2 |\tau_i|^x}{\sum_{i=1}^{I} |\alpha_i(f)|^2}, \tag{27}$$

where $\overline{\tau^x}$ describes the first (x=1) or second (x=2) moment of the instantaneous power-delay profile, respectively. Due to the decrease of the beamwidth in the directional antenna case, the number of significant multipath components decreases. Hence, the rms delay spread reduces from 0.20 ns to 3.2 ps when the directional antenna is used. The coherence bandwidth, which is computed as $0.2/$rms delay spread, reaches 63 GHz when the directional antenna is used. This indicates a very large range of frequencies over which the channel can be considered as flat. For NLoS case, the main beam of the directional antenna is adjusted to the direction of the strongest NLoS (i.e., the direction of the reflected ray 1). Compared with the LoS case, the total power gain is -104.6 dB, which is 30 dB less, and the rms delay spread increases since the scattered rays become significant. Furthermore, the coherence bandwidth reduces to 9.3 GHz.

D. Wideband Channel Capacity

The wideband capacity in the 3D end-to-end model in the THz band can be calculated as:

$$C = \sum_{n=1}^{N} \Delta f \log(1 + \frac{|H_{\text{e2e}}(f_n)|^2 P_n}{\Delta f B_N(f_n)}), \tag{28}$$

where N refers to the total number of sub-bands for transmission, P_n denotes the transmit power in the n^{th} sub-band and the total transmit power $\sum_{n=1}^{N} P_n$ is fixed. H_{e2e} is the transfer function given in (1), and B_N stands for power spectral density of the additive white Gaussian noise. Graphene-based antennas can support wideband transmission, whose bandwidth can reach up to 10% of the carrier frequency [6]. Therefore, we choose three spectral windows to compute the channel capacity, namely, 0.3-0.31 THz, 0.8-0.9 THz and 1.9-2.0 THz. The channel capacity for the different distances with the use of the isotropic antennas and the 13-dB-gain graphene antenna are shown in Fig. 4, and are summarized as follows.

First, the 13-dB-gain antennas at the transmitter and receiver can improve the capacity by an order of 10^2. Second, the higher frequency and wider bandwidth do not always suggest the larger capacity. Due to the high molecular absorption loss at the high THz frequencies such as 1.9-2 THz, the capacity of this band decreases with the distance faster than the other bands. Specifically, the average capacity with the use of 13-dB-gain antennas are 3.8 Gbps, 11.5 Gbps, and 4.0 Gbps, for the frequency bands 0.3-0.31 THz, 0.8-0.9 THz and 1.9-2.0 THz. These values drop to 0.31 Gbps, 0.57 Gbps, and 0.12 Gbps, respectively, when the isotropic antennas are used. Third, a target capacity of 100 Gbps can only be achieved with the directional antenna at high frequency band. The transmitting range is 0.4 m for the 0.8-0.9 THz band. Although 100 Gbps channel capacity is not achieved at 0.3-0.31 THz band, the

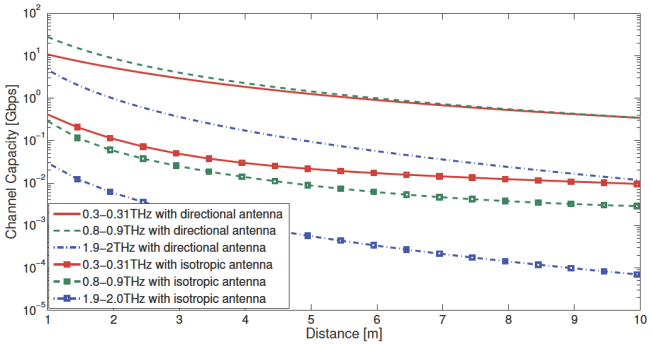

Figure 4: Channel capacity for the different distances.

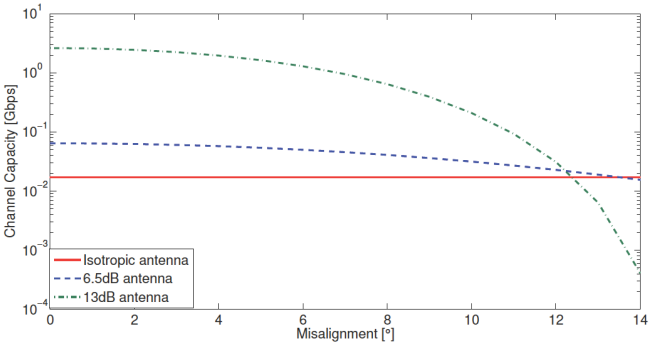

Figure 5: Channel capacity for the different misalignment.

channel capacity is more steady over this band.

E. Antenna Misalignment

In reality, perfect antenna alignment may be not achieved. Antenna misalignments may affect the channel performance. To study the effect of antenna misalignment on the channel performance, we show the channel capacity for the 0.3-0.31 THz band with different antenna gains and level of misalignment in Fig. 5. The misalignment level is evaluated in terms of the angle between the main beam direction and the perfect alignment direction.

Within 14° misalignment, as the misalignment angle increases, the channel capacity decreases considerably, from 2.63 Gbps to 0.41 Mbps, for the 13 dB gain antenna, whereas the 6.5 dB gain antenna are affected only marginally, from 64 Mbps to 12 Mbps. This is caused since the 6.5 dB gain antenna has a wider beamwidth than the 13 dB gain antenna. For the isotropic antenna case, the channel capacity keeps at 17 Mbps for different alignment angles. Specifically, the 6.5 dB gain antenna outperforms the 13 dB gain antenna when the misalignment is larger than 12.2°. When the misalignment angle is 12.4° onwards, the channel capacity of the 13 dB-gain antenna is less than the isotropic case. The compromise between the achieved gain and the misalignment tolerance is an important factor to consider in the system design.

IV. Conclusion

In this paper, we developed a 3D end-to-end model which includes the graphene-based antenna response and the multi-path channel in the THz band. Moreover, the antenna response is validated through the COMSOL simulations. By using the developed model, an in-depth analysis on the 3D channel characteristics is carried out in the THz band. In particular, with the use of a 13 dB gain antenna, the delay spread reduces from 0.2 ns to 3.2 ps and the angular spread reduces by a factor of 100. The resulting coherence bandwidth reaches 63 GHz and the channel capacity can be improved by an order of 10^2. In terms of improving the communication range, a target capacity of 100 Gbps can be achieved with the directional antenna for the distance at 0.4 m by using the 0.8-0.9 THz band, whose bandwidth is 100 GHz, and it is not realizable with the isotropic antenna. However, the use of the directional antenna requires the beam alignment between the transmitter and the receiver. When the misalignment angle exceeds 12.4°, the channel capacity of the 13 dB gain antenna is less than the isotropic case. Ultimately, this work lays out the foundation for reliable and efficient ultra-high-speed wireless communications in the THz band.

Acknowledgment

The authors would like to thank Dr. Josep Miquel Jornet and A. Ozan Bicen for their constructive criticism.

This work was supported by the U.S. National Science Foundation (NSF) under Grant No. CCF-1349828 and in part by Alexander von Humboldt Foundation through Dr. Ian F. Akyildiz's Humboldt Research Prize in Germany.

References

[1] T. Kleine-Ostmann and T. Nagatsuma, "A review on terahertz communications research," *Journal of Infrared, Millimeter and Terahertz Waves*, vol. 32, no. 2, pp. 143–171, 2011.

[2] I. F. Akyildiz, J. M. Jornet, and C. Han, "Terahertz band: Next frontier for wireless communications," *Phyiscal Communication (Elsevier) Journal*, vol. 12, pp. 16–32, Sept 2014.

[3] S. Priebe, M. Kannicht, M. Jacob, and T. Kurner, "Ultra Broadband Indoor Channel Measurements and Calibrated Ray Tracing Propagation Modeling at THz Frequencies," *IEEE Journal of Communications and Networks*, vol. 15, no. 6, pp. 547–558, 2013.

[4] C. Han, A. O. Bicen, and I. F. Akyildiz, "Multi-ray channel modeling and wideband characterization for wireless communications in the thz band," *IEEE Transactions on Wireless Communications*, vol. 14, no. 5, pp. 2402–2412, May 2015.

[5] P. Burke, S. Li, and Z. Yu, "Quantitative theory of nanowire and nanotube antenna performance," *IEEE Transactions on Nanotechnology*, vol. 5, no. 4, pp. 314–334, Jul. 2006.

[6] J. M. Jornet and I. F. Akyildiz, "Graphene-based plasmonic nano-antennas for terahertz band communication in nanonetworks," *IEEE Journal on Selected Areas in Communications*, vol. 31, no. 12, pp. 685–694, December 2013.

[7] M. Tamagnone, J. S. Gómez-Díaz, J. R. Mosig, and J. Perruisseau-Carrier, "Analysis and design of terahertz antennas based on plasmonic resonant graphene sheets," *Journal of applied physics*, 2012.

[8] COMSOL, "COMSOL Multiphysics Simulation Software." [Online]. Available: http://www.comsol.com/products/multiphysics/

[9] J. Jornet and I. Akyildiz, "Channel modeling and capacity analysis for electromagnetic wireless nanonetworks in the terahertz band," *IEEE Transactions on Wireless Communications*, vol. 10, no. 10, 2011.

[10] R. Piesiewicz, C. Jansen, D. Mittleman, T. Kleine-Ostmann, M. Koch, and T. Kurner, "Scattering Analysis for the Modeling of THz Communication Systems," *IEEE Transactions on Antennas and Propagation*, vol. 55, no. 11, pp. 3002–3009, Nov. 2007.

[11] H. Ragheb and E. R. Hancock, "The Modified Beckmann–Kirchhoff Scattering Theory for Rough Surface Analysis," *Pattern Recognition (Elsevier) Journal*, vol. 40, no. 7, pp. 2004–2020, 2007.